

Utilizing Er-doped ZnIn₂S₄ for efficient photocatalytic CO₂ conversionFanghe Zhou^{a,1}, Yonglin Zhang^{a,1}, Jiang Wu^{a,*}, Wu Yang^a, Xu Fang^a, Tao Jia^b, Yang Ling^c, Ping He^a, Qizhen Liu^{d,**}, Jia Lin^{e,*}^a College of Energy and Mechanical Engineering, Shanghai University of Electric Power, Shanghai 200090, China^b State Key Laboratory of Pollution Control and Resources Reuse, College of Environmental Science and Engineering, Tongji University, Shanghai 200092, China^c Institute of Photochemistry and Photofunctional Materials, University of Shanghai for Science and Technology, Shanghai 200093, China^d Shanghai Environmental Monitoring Center, Shanghai 200235, China^e College of Mathematics and Physics, Shanghai University of Electric Power, Shanghai 200090, China

ARTICLE INFO

Keywords:

ZnIn₂S₄

Erbium-doping

Photocatalytic CO₂ Reduction

DFT

ABSTRACT

In the quest for effective photocatalysts for CO₂ reduction, catalysts doped with rare-earth elements have garnered considerable attention due to their unique electronic structures and energy levels, which enable enhanced light absorption and charge transfer capabilities. In this study, we synthesized erbium-doped ZnIn₂S₄ using a hydrothermal method. Compared with pure ZnIn₂S₄, the erbium-doped variant displayed a significant boost in photocatalytic performance, improving the efficiency of CO₂ reduction to methane by 256 times, with a selectivity exceeding 90 % towards methane. Through DFT analysis, we found that the doping of erbium introduced new energy levels into ZnIn₂S₄, effectively narrowing the band gap and thereby enhancing light absorption efficiency. Furthermore, our research revealed that erbium-doped ZnIn₂S₄ introduces a uniquely distinct reaction pathway for CO₂ reduction compared to pure ZnIn₂S₄, significantly reducing the reaction barrier. Moreover, it enhances the adsorption of the key intermediate, *CHO and *CH₂O, steering the reaction pathway towards the production of CH₄. These findings not only offer valuable insights for the development of efficient and selective photocatalysts but also pave new avenues for research into CO₂ conversion.

1. Introduction

In the face of escalating global climate change and environmental pressures, the effective reduction and utilization of atmospheric carbon dioxide (CO₂) has become a pressing research topic [1]. A promising approach lies in the photocatalytic conversion of CO₂, where solar energy is harnessed to transform atmospheric CO₂ into valuable chemicals and fuels, thus enabling carbon recycling [2]. This approach not only offers superior energy efficiency but also provides a green solution to the carbon emissions problem [3]. However, a major challenge confronting this field is the development and selection of efficient photocatalysts, particularly those that demonstrate high performance under a broad spectrum of light irradiation [4].

Zinc indium sulfide (ZnIn₂S₄), a two-dimensional layered structure falling under the category of metal thio-spinels, has received considerable attention owing to its extraordinary photocatalytic activity and environmental durability [5]. Its distinctive feature, a moderate band

gap, permits ZnIn₂S₄ to effectively utilize the visible fraction of sun light, thereby augmenting its photocatalytic efficiency. However, rapid recombination of photogenerated electron-hole pairs and low migration capability hinders the wider application of ZnIn₂S₄ in photocatalysis [6]. The fast recombination of photogenerated carriers limits the charge separation efficiency, thereby curtailing the full exploitation of its photocatalytic potential [7]. Consequently, considerable research efforts are dedicated to suppressing carrier recombination and promoting charge pair separation in order to enhance the photocatalytic performance of ZnIn₂S₄ through structural modification. Strategies such as doping with appropriate elements, creating defect structures, or developing composite materials have been explored to overcome these limitations, with each approach offering its own set of advantages and challenges [8].

Rare earth elements, due to their unique electronic structures, present a compelling alternative to traditional transition metal dopants in enhancing photocatalytic performance [9]. With their distinctive f-block

* Correspondence to: No. 2103 Pingliang Road, Shanghai 200090, China.

** Correspondence to: No. 55 Sanjiang Road, Shanghai 200235, China.

E-mail addresses: wjcf2002@163.com (J. Wu), liuqz@sheemc.cn (Q. Liu), jlin@shiep.edu.cn (J. Lin).¹ These authors contributed to the work equally and should be regarded as co-first authors.

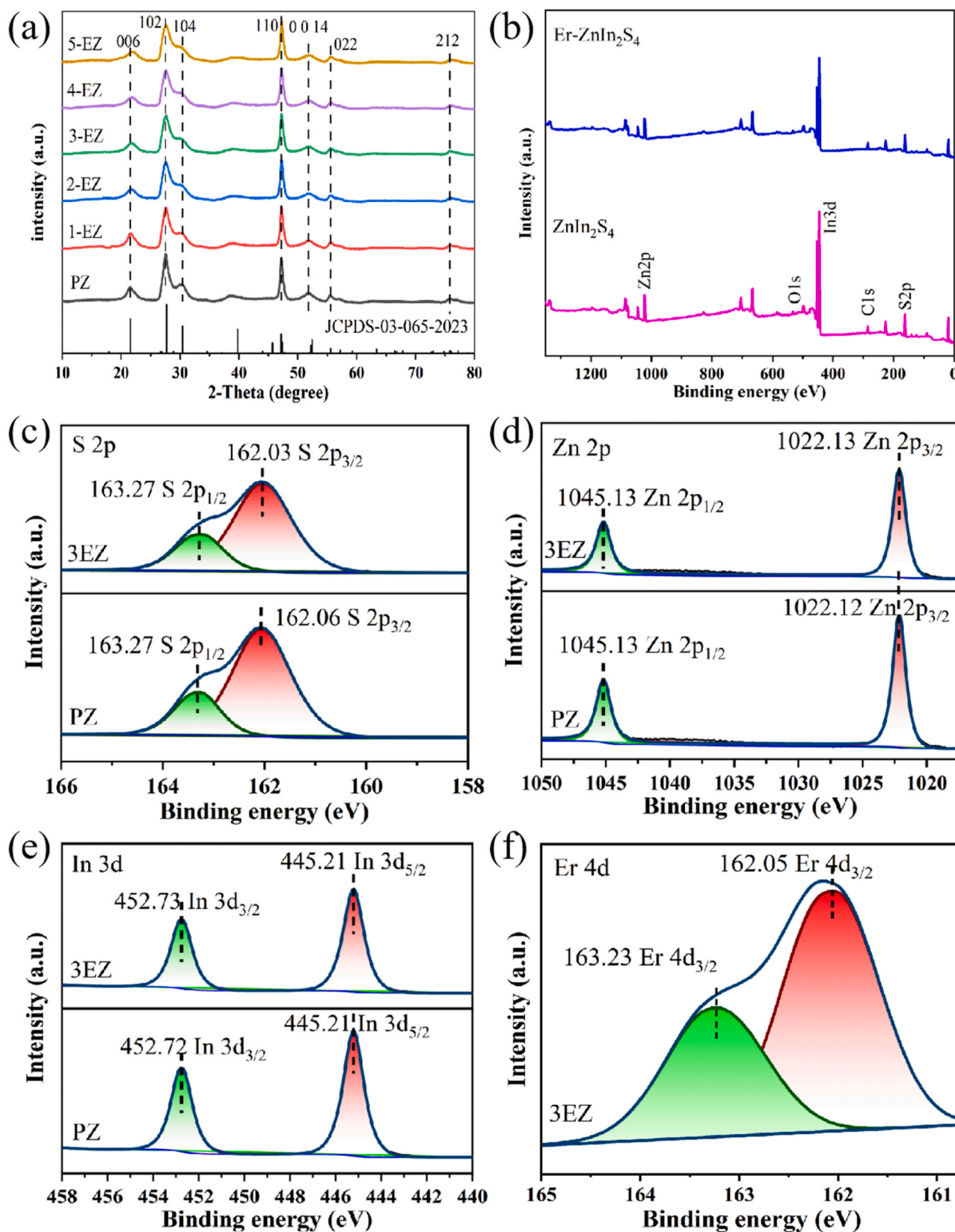


Fig. 1. XRD patterns of samples (a), XPS survey (b), High-resolution XPS spectra of samples (c-f).

electrons and variable oxidation states, rare earth elements provide a wider range of possible energy levels that can participate in the charge transfer processes, potentially leading to more efficient separation of photo-induced electron-hole pairs and consequently higher photocatalytic performance [10]. Furthermore, the introduction of rare earth elements could potentially influence the physical and chemical properties of the photocatalyst, such as optical absorption, electronic conductivity, and chemical stability, thereby providing another means to optimize the photocatalytic performance. In this context, Erbium (Er) stands out as a notable member of the lanthanide series of the rare earth elements [11]. Er is frequently used as a dopant in photocatalytic applications due to its unique intra-4 f shell transitions that can produce a photoemission at $1.54\ \mu\text{m}$ [12]. This characteristic emission, combined with its ability to convert infrared (IR) light to visible light, allows Er to extend the light absorption range and boost the utilization of solar energy. Upon incorporation into ZnIn_2S_4 , Er could significantly modify the host material's electronic structure and introduce new energy levels. These changes could facilitate more efficient separation of photo-generated carriers, thereby enhancing the photocatalytic activity [13]. The unique properties of Er, combined with the inherent advantages of ZnIn_2S_4 , position Er-doped ZnIn_2S_4 as a promising candidate warranting

further exploration in the field of photocatalytic CO_2 conversion [14].

Existing research on Er-doped catalysts attests to their superior performance in photocatalysis. For instance, a study by Wei et al. reported the synthesis of Er^{3+} doped BiOBr , which was employed for photocatalytic degradation of Rhodamine B (RhB) [15]. Their findings revealed a significant enhancement in efficiency, with the doped BiOBr outperforming its pure counterpart by a factor of 2.7. Similarly, a study conducted by Mohamed et al. using the GGA + U method investigated the electronic structure and optical properties of an Er-doped ZnO system [16]. Their computational results illustrated that Er-doping effectively improved the magneto-optical properties of the catalyst. Despite these promising results, a more comprehensive understanding of the precise mechanisms behind Er-doped catalysts in photocatalytic CO_2 conversion remains largely unexplored. The opportunities and challenges associated with the introduction of rare-earth elements into photocatalysts warrant further examination. Furthermore, due to the large atomic radius of rare-earth elements and their strong electronic orbital coupling, coupled with complex electronic structures, density functional theory (DFT) calculations for these systems become significantly more challenging.

Herein, we report the synthesis of Er-doped zinc sulfide using the

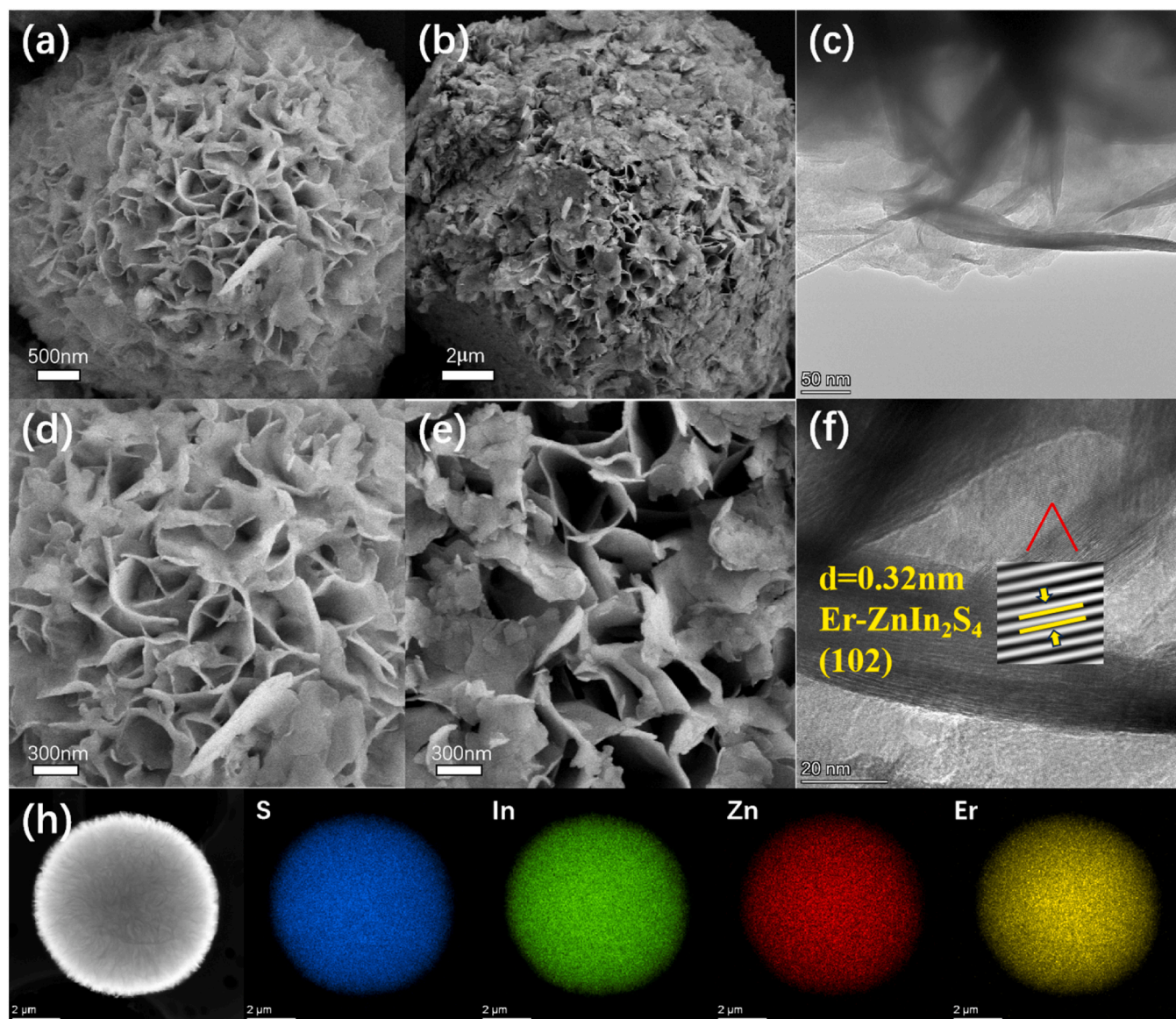


Fig. 2. SEM of (a, d) ZnIn_2S_4 and Er-ZnIn₂S₄ (b, e), TEM of Er-ZnIn₂S₄ (c, f), and corresponding elemental mappings of Er-ZnIn₂S₄ (g, h).

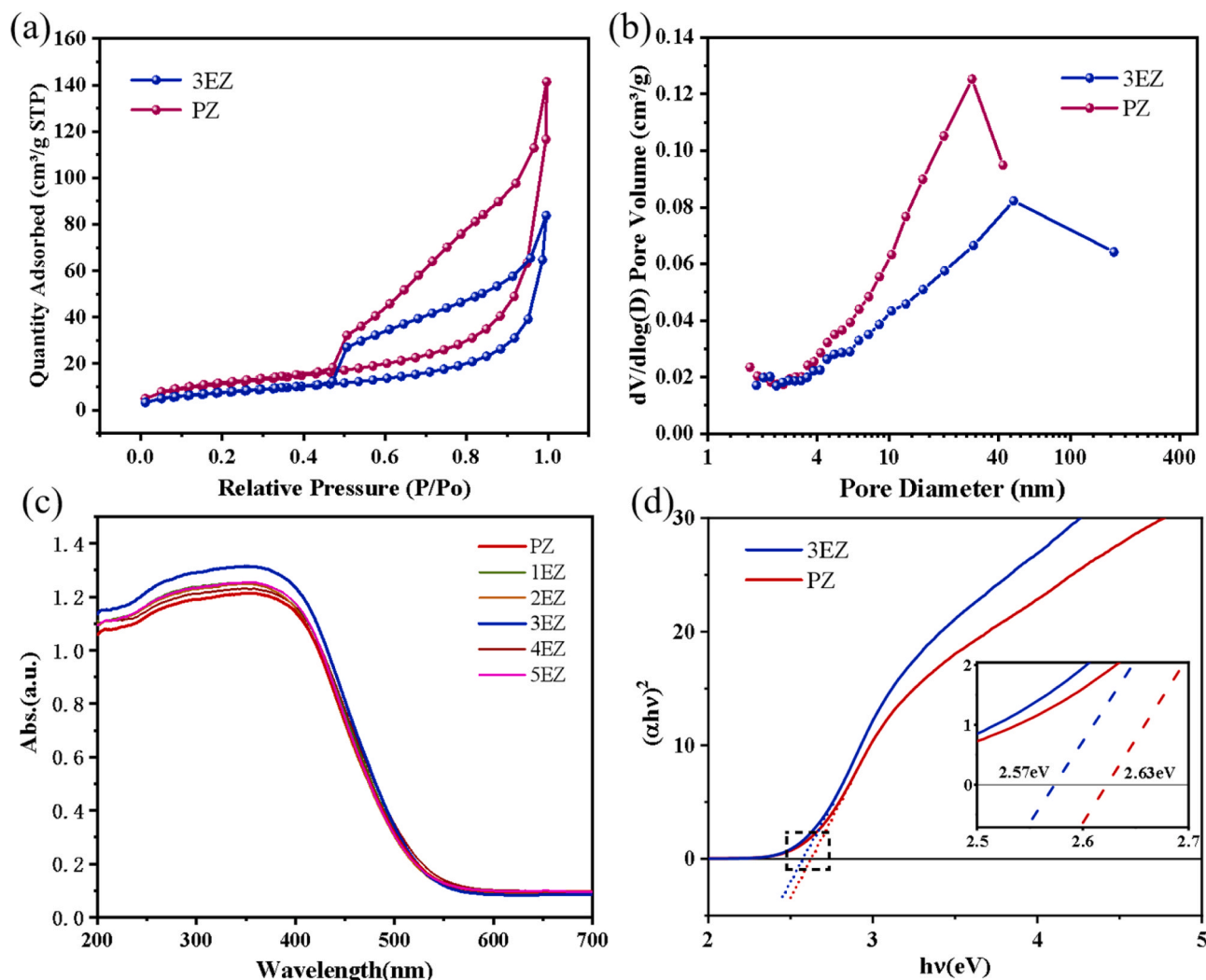


Fig. 3. CO₂ adsorption-desorption isotherms (a), Pore diameter distribution (b), Optical absorption spectra (c) and Tauc plots (d).

hydrothermal method, and verify its photocatalytic properties for CO₂ reduction under visible light irradiation. A comprehensive examination of the impacts of Er doping on the catalyst's crystal structure, electronic properties, and visible light-driven photocatalytic CO₂ reduction activity is conducted from both experimental and theoretical perspectives. By integrating computational and experimental approaches, we delve into the reasons why the Er-doped samples exhibit enhanced photocatalytic reduction performance for CO₂ and significant suppression of hydrogen evolution reaction. These findings provide valuable insights for the development of efficient and selective photocatalysts for carbon dioxide transformation and pave the way for novel avenues in this research field.

2. Experimental & computational methods

2.1. Experimental

2.1.1. Materials

The chemicals utilized in this experiment, including Zinc chloride (ZnCl₂), Indium(III) chloride tetrahydrate (InCl₃·4 H₂O), Thiourea (C₂H₅NS), Erbium nitrate pentahydrate (Er(NO₃)₃·5 H₂O), and Cetyltrimethylammonium bromide (C₁₉H₄₂BrN), were procured from Shanghai Titan Technology Co., Ltd. All reagents were of analytical grade and were used without any further purification.

2.1.2. Synthetic steps

Er-doped ZnIn₂S₄ was synthesized employing a hydrothermal approach. Initially, 20 mL of deionized water and 20 mL of anhydrous ethanol were combined in a beaker and stirred until completely dissolved. Subsequently, ZnCl₂ (2 mmol), InCl₃·4 H₂O (4 mmol), Er(NO₃)₃·5 H₂O, C₂H₅NS (6 mmol), and C₁₉H₄₂BrN (0.2 g) were added sequentially while stirring continued. Five sets were prepared with molar ratios of Er(NO₃)₃·5 H₂O to ZnIn₂S₄ being 1:9, 2:8, 3:7, 4:6, and 5:5, denoted as 1EZ, 2EZ, 3EZ, 4EZ, and 5EZ, respectively. The mixture was magnetically stirred until fully dissolved, during which time the solution transitioned from turbidity to clarity and then back to turbidity. Next, the hydrothermal reactor containing the mixed suspension was heated at 160 °C for 18 h. The resultant precipitate was collected by centrifugation following natural cooling and was then rinsed three times with deionized water and thrice with ethanol. The final powder was dried at 80 °C for 12 h. ZnIn₂S₄, denoted as PZ, was prepared using the same method for comparison purposes.

For details of the photocatalytic experiments, please refer to the [Supporting Information](#).

2.2. Characterization techniques & computational methods

For detailed characterization techniques and computational methods, please refer to the [Supporting Information](#) [17–20].

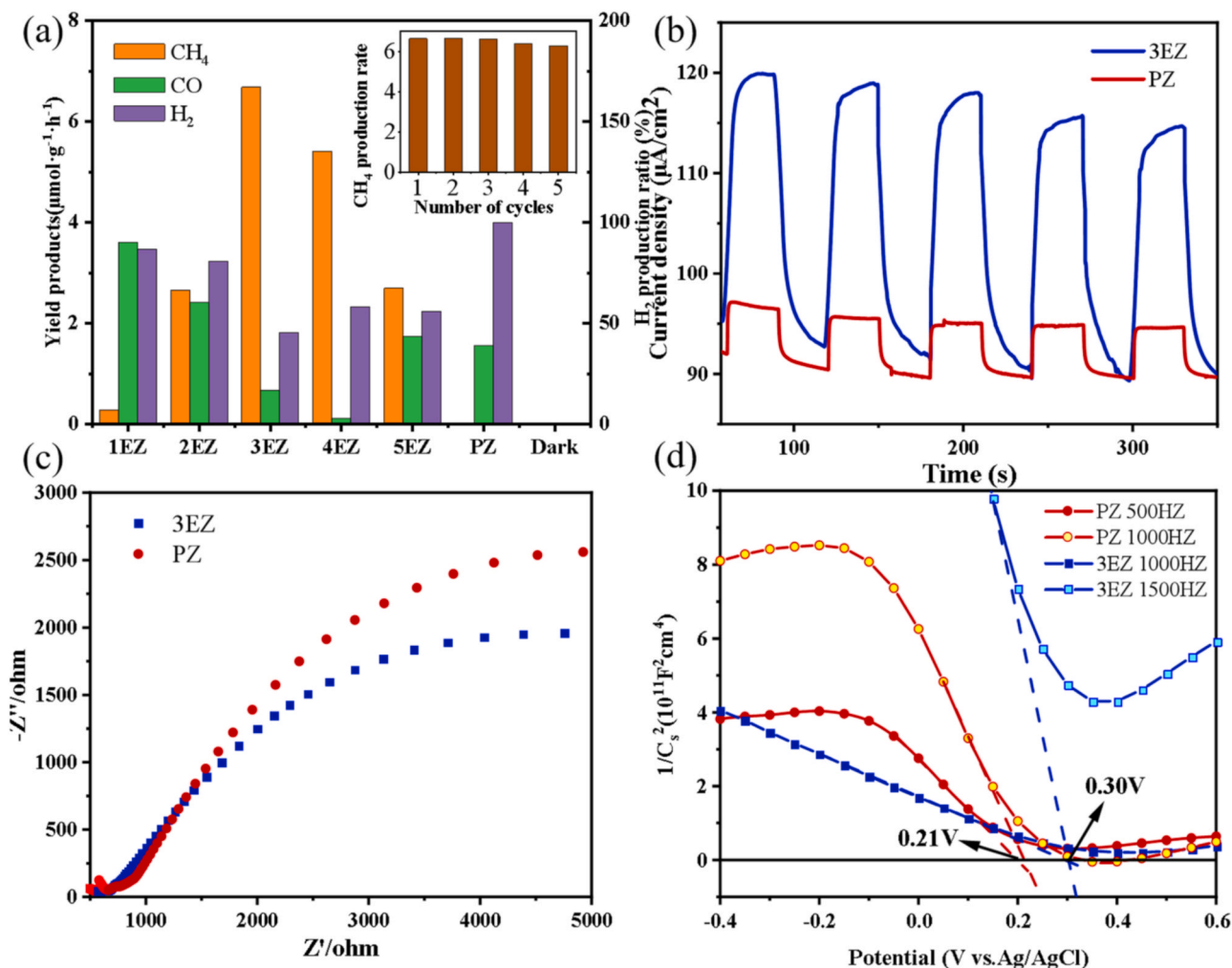


Fig. 4. CO_2 reduction efficiency (a), transient photocurrent density (b), Electrochemical Impedance Spectroscopy Nyquist plot (c) and Mott-Schottky plots (d).

3. Results and discussions

3.1. Structural characterization

In order to investigate the crystal phase and structure of the synthesized samples, X-ray diffraction (XRD) measurements were conducted [21]. The resulting diffraction patterns are displayed in Fig. 1a. The majority of the observed peaks align well with those in the standard card, confirming the primary phase of the sample as ZnIn_2S_4 . Notably, no conspicuous peaks deviating from the main ones are detected, suggesting the absence of discernible impurities and indicating that Er doping does not detrimentally affect the pristine ZnIn_2S_4 crystal structure. The crystallite sizes of the samples were estimated from the full width at half maximum (FWHM) of the (110) peak located around $\sim 47.2^\circ$, employing the Scherrer equation [22]. For the pure ZnIn_2S_4 , the FWHM is 0.59° , yielding an approximate crystallite size of 2.56 nm. In contrast, for the Er-doped ZnIn_2S_4 , the FWHM is 0.65° , corresponding to a slightly reduced crystallite size of about 2.33 nm. This slight broadening of the (110) peak and the corresponding reduction in crystallite size in the Er-doped ZnIn_2S_4 compared to the pure ZnIn_2S_4 may indicate that the incorporation of Er introduces some lattice distortions or stresses, resulting in a decrease in the crystallite size.

Surface chemical composition of both pure ZnIn_2S_4 and Er- ZnIn_2S_4 nanospheres was characterized using XPS spectroscopy (as shown in Fig. 1b-f). The presence of Zn, In, and S elements is clearly observed in the pure ZnIn_2S_4 sample. Notably, the characteristic peak energies of Zn,

S, and In in the Er-doped ZnIn_2S_4 were found to be nearly identical to those in pure ZnIn_2S_4 , with negligible alterations in peak width and shape [23]. This implies that the chemical environment or oxidation states of Zn, S, and In remained predominantly unchanged following Er doping. Nevertheless, a discernible decrease in the intensities of the Zn, S, and In peaks was observed in the Er-doped ZnIn_2S_4 when compared to the pure ZnIn_2S_4 . This observation suggests that the incorporation of Er likely substitutes a fraction of Zn, S, or In sites, consequently leading to a diminished relative concentration of these elements. Upon closer inspection, the energy positions of the two primary peaks of Er 4d ($4d_{3/2}$ and $4d_{5/2}$) were found to align closely with the energy position of the S 2p peaks. This could hint at a possible chemical interaction occurring between Er and S. Moreover, the appearance of the Er 4d peaks provided unequivocal evidence of successful Er doping [24].

Fig. 2 presents the scanning electron microscopy (SEM) images and the corresponding mapping spectra of ZnIn_2S_4 and Er-doped ZnIn_2S_4 . As depicted in Fig. 2a, ZnIn_2S_4 exhibits a uniform, porous, flower-like structure with an average diameter of 5–6 μm . A higher resolution SEM image of ZnIn_2S_4 , shown in Fig. 2d, reveals that this porous nano-flower structure is composed of a multitude of accumulated nanosheets [25]. The SEM images of Er-doped ZnIn_2S_4 , shown in Fig. 2b and e, indicate that the introduction of Er significantly enlarges the diameter of the whole particulate structure to approximately 16–18 μm . This enlargement can be attributed to changes in the crystal growth rate induced by the Er doping, resulting in a larger particle size for Er-doped ZnIn_2S_4 [26]. The incorporation of Er also partially disrupts the initially

uniform porous structure. Nevertheless, the flower-like structure still comprises a plethora of minute nanosheets. The high-resolution image reveals that the size and thickness of the nanosheets composing the Er-ZnIn₂S₄ flower-like structure are largely similar to those constituting the pure ZnIn₂S₄ structure.

Although Er doping does not alter the nanoflower-like spherical morphology of ZnIn₂S₄, the enlargement of the flower-like particles leads to a reduction in the specific surface area of the samples. Comparative analysis of the adsorption-desorption isotherms for PZ and 3EZ (Fig. 3a) reveals that both materials exhibit H4-type hysteresis loops. While the adsorption curve for 3EZ closely resembles that of PZ, the adsorption capacity at all relative pressures is slightly lower for 3EZ, resulting in a significantly smaller hysteresis loop area. This implies that PZ possesses a higher specific surface area and a more complex pore structure. Data from the pore size distribution (Fig. 3b) further corroborates that although Er-ZnIn₂S₄ has a broader range of pore diameters and larger maximum pore size compared to PZ, PZ exhibits greater pore volumes within certain size ranges. In summary, the enhanced yield in Er-doped ZnIn₂S₄ is not attributable to a higher specific surface area. Instead, erbium doping profoundly alters the electronic structure of the material, thereby improving its catalytic efficiency. This is further substantiated in subsequent characterization experiments and DFT calculations concerning the CO₂ reduction mechanism.

The microstructure of the Er-doped ZnIn₂S₄ material was characterized using transmission electron microscopy (TEM). Detailed observation of the edges of the microspheres enabled us to identify the specific structure of the nanosheets, as shown in Fig. 2c and f [27]. The enlarged high-resolution TEM image inset in Fig. 2f reveals the lattice fringes of Er-ZnIn₂S₄. Upon measuring these fringes and comparing them with standard cards, we identified the lattice spacing of 0.32 nm to correspond to the (102) plane of hexagonal Er-ZnIn₂S₄ [28]. It is noteworthy that the lattice spacing of Er-doped ZnIn₂S₄ closely resembles that of pure ZnIn₂S₄. This suggests that the incorporation of Er may induce minor lattice distortions but does not significantly alter the morphology of ZnIn₂S₄. These observations are in agreement with the findings from X-ray diffraction spectra. As illustrated in Fig. 2h, the elements S, In, Zn, and Er are uniformly distributed throughout the microsphere sample. These observations indicate that Er³⁺ ions are homogeneously doped into the ZnIn₂S₄ material, corroborating the XPS results [29].

3.2. Er-ZnIn₂S₄ catalytic performance

Building upon the comprehensive characterization of our samples, we next sought to evaluate their photocatalytic activity in the context of CO₂ reduction under simulated sunlight. For this purpose, 50 mg of 3Er-ZnIn₂S₄ was combined with 10 mL of triethanolamine in a 90 mL mixture of deionized water. Ultrasonic treatment was utilized to ensure thorough dispersion of the catalyst in the solution. Triethanolamine served as a sacrificial electron donor within this photocatalytic CO₂ reduction system. The performance of the photocatalyst under simulated sunlight is illustrated in Fig. 4a, which presents a histogram of product yield over a 6-hour testing period, with samples taken every hour. The principal products observed were CO and CH₄. Concurrently, we performed control experiments to verify the source of carbon in the reduction products. When no CO₂ gas was present, no significant reduction products were detected, confirming that the carbon in the reduction products originates from CO₂. Further, in the absence of either light or a catalyst, no reduction products were detected, underscoring the necessity of both light and the catalyst for the photocatalytic reduction of CO₂ [21].

It was observed that the pristine ZnIn₂S₄ exhibited relatively low photocatalytic activity for the reduction of CO₂. The primary product was CO, with a yield of 1.56 $\mu\text{mol}\cdot\text{g}^{-1}\cdot\text{h}^{-1}$, while the yield of CH₄ was only 0.026 $\mu\text{mol}\cdot\text{g}^{-1}\cdot\text{h}^{-1}$. The introduction of a small amount of Er dopant had a slight promotional effect on the production of CO.

However, as the Er doping level increased, the yield of CH₄ gradually increased, peaking and then slowly declining. The Er-doped ZnIn₂S₄, denoted as 3EZ, displayed optimal photocatalytic performance, achieving a CH₄ yield of 6.68 $\mu\text{mol}\cdot\text{g}^{-1}\cdot\text{h}^{-1}$ - 256 times that of the undoped ZnIn₂S₄. This indicates not only that Er enhances the photocatalytic performance of ZnIn₂S₄ but also that Er has selectivity towards CH₄. After doping ZnIn₂S₄ with Er, the yield of CH₄ significantly increased, with a selectivity of over 90 %.

Moreover, it's clear that 3EZ exhibited the most potent inhibitory effect on the production of H₂, with a yield at 45 % of that of the pure sample. This is calculated based on the H₂ yield of pristine ZnIn₂S₄, indicating that Er-doped ZnIn₂S₄ has an inhibitory effect on H₂ production. Furthermore, we conducted a long-cycle test on 3EZ (five cycles, each lasting six hours). As can be seen clearly in Fig. 4a, after five consecutive cycles, the CH₄ yield from 3EZ decreased slightly. However, even after 30 h, it maintained a CH₄ yield of 6.26 $\mu\text{mol}\cdot\text{g}^{-1}\cdot\text{h}^{-1}$, representing 93 % of the initial yield, demonstrating that 3EZ maintained excellent photocatalytic activity after 30 h of testing. In supplementary experiments, we prepared Nd-, Gd-, and La-doped ZnIn₂S₄ catalysts using the same doping ratios as those used for the 3EZ sample (Fig. S1), in order to make a direct comparison with the Er-doped catalyst (3EZ). However, in parallel photocatalytic tests, these catalysts did not exhibit the same efficacy in CO₂ reduction as the Er-doped ZnIn₂S₄. They produced negligible amounts of CH₄ and had very limited yield of CO. Additionally, all of these supplemental catalysts generated a certain amount of H₂, indicating their inability to resist the competition between the HER and CO₂RR. The reason for this is that HER has a lower energy barrier, which leads to diminished product selectivity. This highlights the unique and superior performance of Er-doped ZnIn₂S₄.

We conducted a series of electrochemical tests on the materials. As shown in Fig. 4b, the photocurrent results for PZ and 3EZ clearly demonstrate that doping with erbium ions significantly enhances the photocurrent. Fig. 4c presents the impedance of PZ and 3EZ, where it is evident that the impedance of 3EZ is smaller relative to PZ. This finding suggests that charge carriers can react more smoothly with surface CO₂. Finally, as shown in Fig. 4d, Mott-Schottky tests were conducted on both samples. The negative slopes of the voltage-capacitance curves for both PZ and 3EZ further confirm that the doping of Er does not alter the p-type semiconductor nature of ZnIn₂S₄. The flat band voltage for the doped 3EZ sample is 0.30 V, higher than that of PZ at 0.21 V. This indicates that 3EZ possesses a stronger internal electric field, which is conducive to the rapid separation and migration of charge carriers. Furthermore, the optical absorption spectra (Fig. 3c) clearly show that Er doping effectively enhances the sample's absorption capabilities within the visible light range. The band gaps (E_g) for PZ (2.63 eV) and 3EZ (2.57 eV) were determined using Tauc plots (Fig. 3d). The reduction in the band gap for the 3EZ sample can be attributed to the introduction of new energy levels by Er doping. In the context of p-type doping, Er accepts electrons from the valence band, creating a shallow 'acceptor level' near the top of the valence band. This facilitates the easier transition of holes from the valence band to this new acceptor level, resulting in a reduced band gap.

3.3. Electronic and structural properties

To unravel the complexities of the structural and electronic attributes of Er-doped ZnIn₂S₄ and its photocatalytic CO₂ reduction mechanism, we employed density functional theory (DFT) calculations [30]. A crucial aspect of our investigation was determining Er's specific substitution site within the ZnIn₂S₄ lattice, which significantly influences the system's inherent properties and subsequent performance. Er exhibits a higher likelihood of substituting Zn or In rather than S within the lattice, primarily due to the atomic radius and electronic configuration. Er shares a similar atomic radius with Zn and In, significantly differing from S, facilitating Er's seamless integration into the Zn or In lattice sites, thereby maintaining structural consistency [31]. Additionally, the

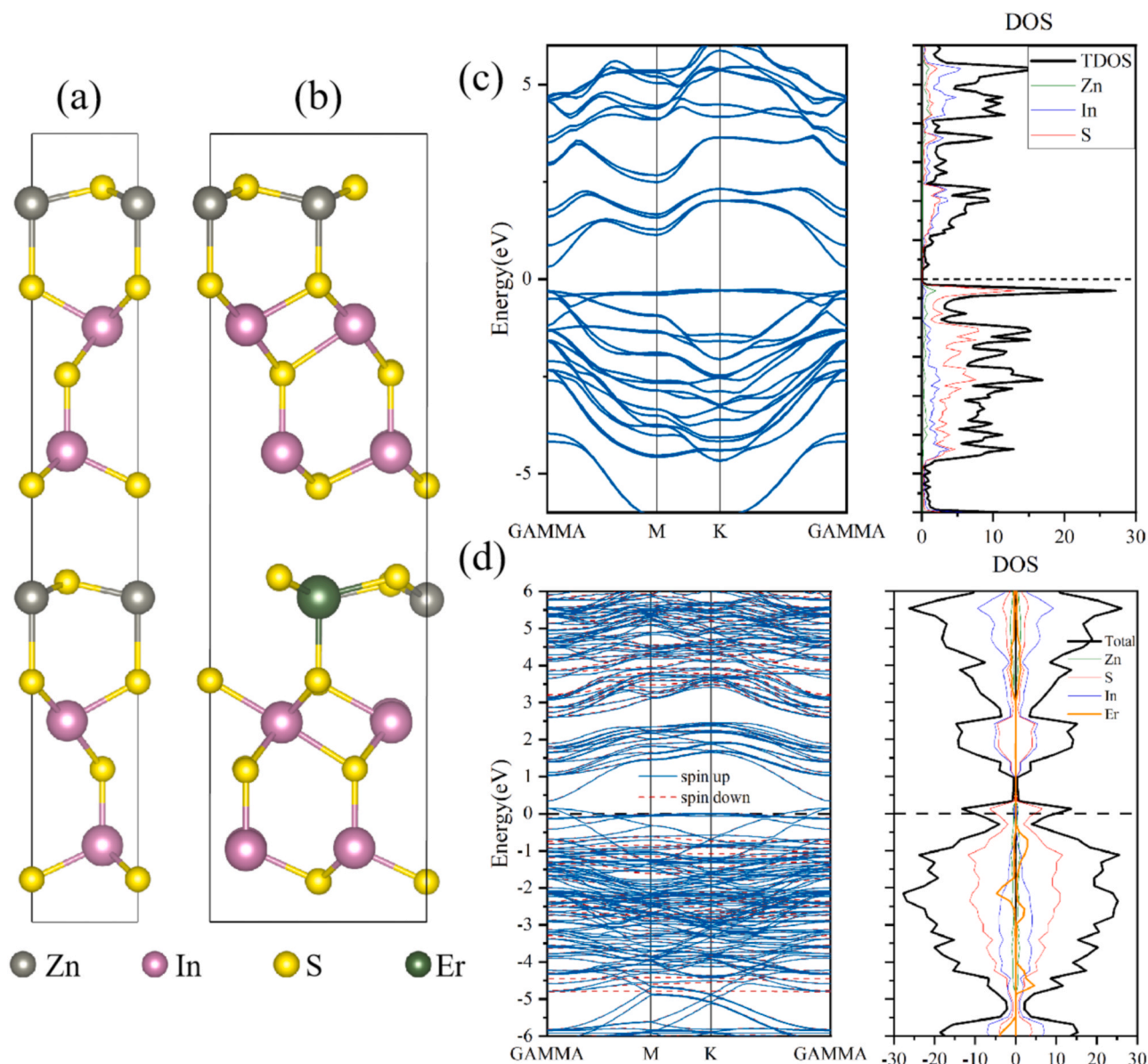


Fig. 5. Crystal structure model of Er-doped ZnIn₂S₄ (a, b), band structure of ZnIn₂S₄ (c) and Er-doped ZnIn₂S₄ (d).

electronic configuration provides insight. Erbium, an f-block element, has outer electronic energy levels similar to those of Zn and In, d-block and p-block elements, respectively. This alignment favors Er's substitution of Zn or In. In contrast, the disparity in valence electron energy levels between Er and sulfur, a p-block element, makes the latter less likely for substitution. To ascertain whether Er primarily substitutes Zn or In, we conducted formation energy calculations (Fig. S2). The data revealed a formation energy of -6.08 eV for Er replacing Zn and -4.32 eV for Er replacing In, conclusively indicating that Er dopants are more likely to occupy Zn sites over In [32].

We employed the DFT+U method to estimate the band gap of the model, aiming to assess the impact of Er doping. Although the use of a U-value correction cannot entirely eliminate the underestimation of the band gap, comparing the changes in the band gap across doped systems using the same method remains a reliable approach. The band structure of the Er-doped system was calculated and compared with the undoped ZnIn₂S₄ to elucidate the distinct electronic-level alterations instigated by Er doping (Fig. 5c, d). For the pure ZnIn₂S₄, the Fermi level is at 2.89 eV, with the Valence Band Maximum (VBM) at 2.62 eV and the Conduction Band Minimum (CBM) at 3.19 eV, leading to a bandgap of 0.57 eV,

indicative of its semiconducting nature. Upon the incorporation of Er, the material undergoes a substantial transformation due to the pronounced localizing effects of the 4f electrons of Er. These electrons interact with the extant electronic states within the valence and conduction bands, introducing new energy levels and thus restructuring the electronic landscape. The band gap in the doped system was effectively reduced, leading to enhanced photocatalytic performance. Through the analysis of the density of states and band calculations, it was observed that in the presence of spin-orbit coupling, the energy bands of the Er-doped system bifurcate into spin-up and spin-down components. Notably, in the conduction band region, the spin-up and spin-down bands overlap almost entirely. This suggests that the influence of the 4f electrons of Er on the conduction band is minimal, likely due to their localized nature limiting hybridization with the s, p, and d orbitals of other elements. However, significant disparities were observed in the valence band. Calculations of the projected density of states (PDOS) indicated these disparities primarily stem from the influence of the localized 4f electrons of Er. Due to their inherently high localization, the 4f electrons are prone to forming covalent or ionic bonds with adjacent atomic orbitals, thereby substantially affecting the energy-level

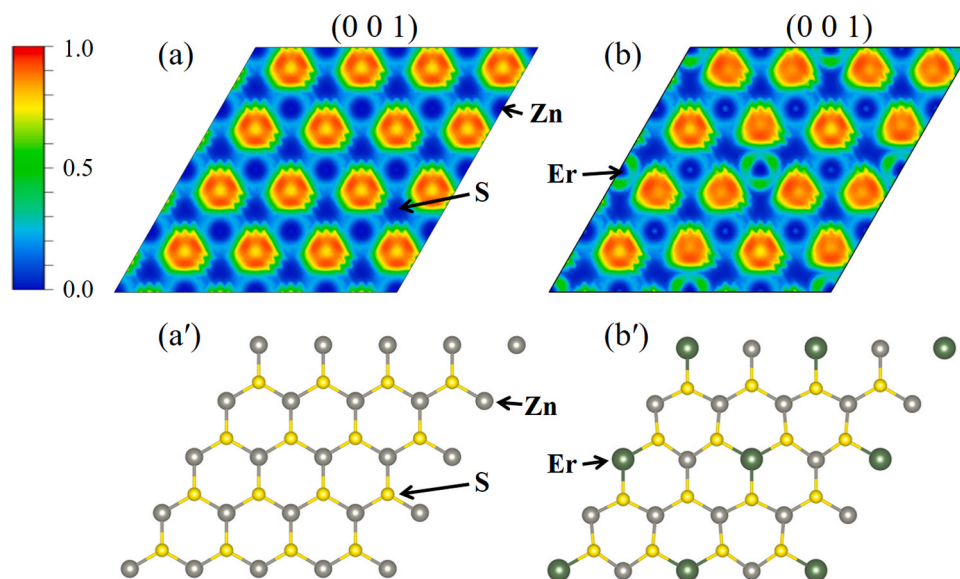


Fig. 6. ELF of ZnIn₂S₄ (a, a') and Er-doped ZnIn₂S₄ (b, b').

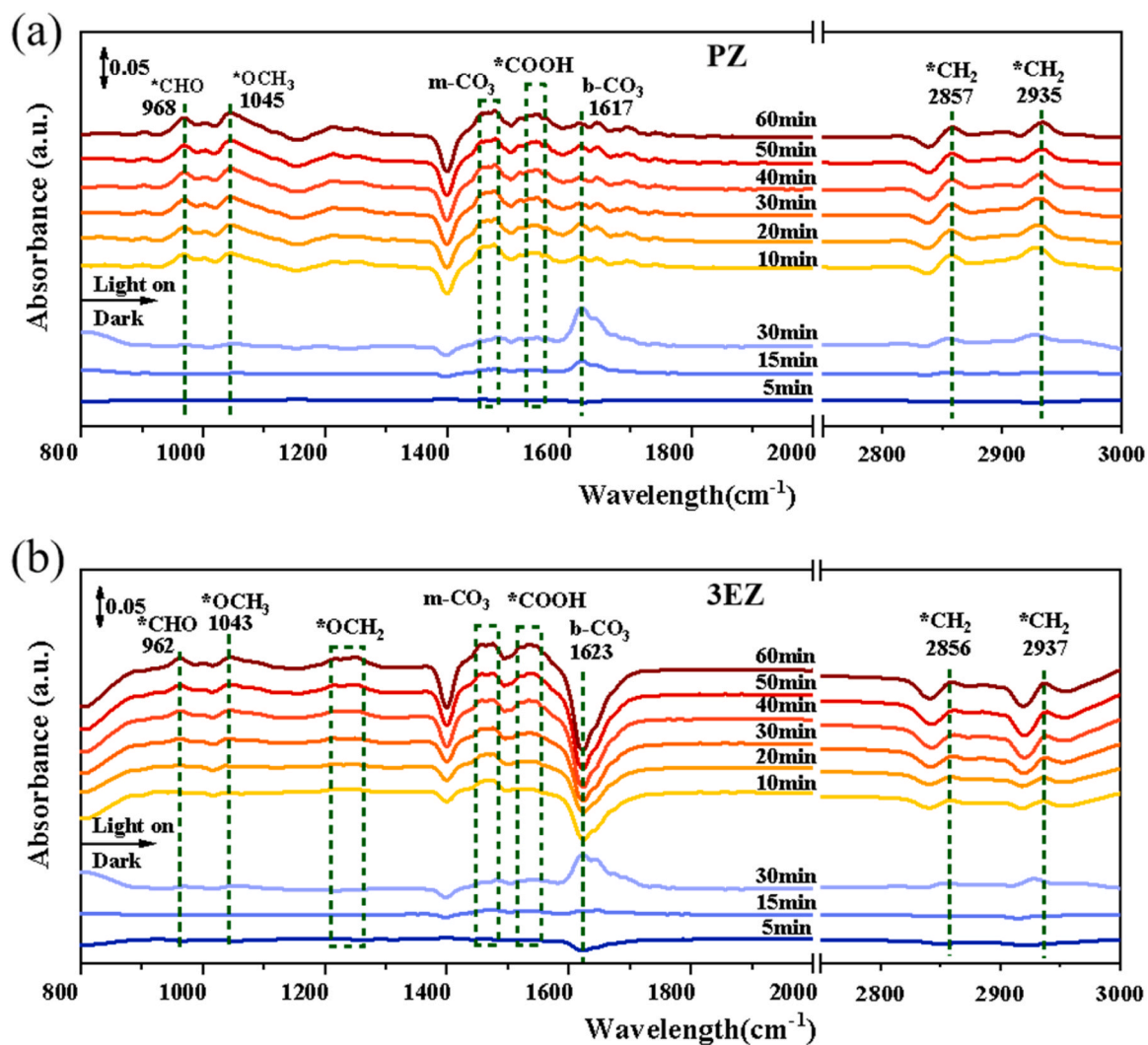


Fig. 7. Time-Resolved In Situ DRIFTS Spectra of PZ (a) and 3EZ (b) Under Xe Lamp Illumination for Durations of 60 min.

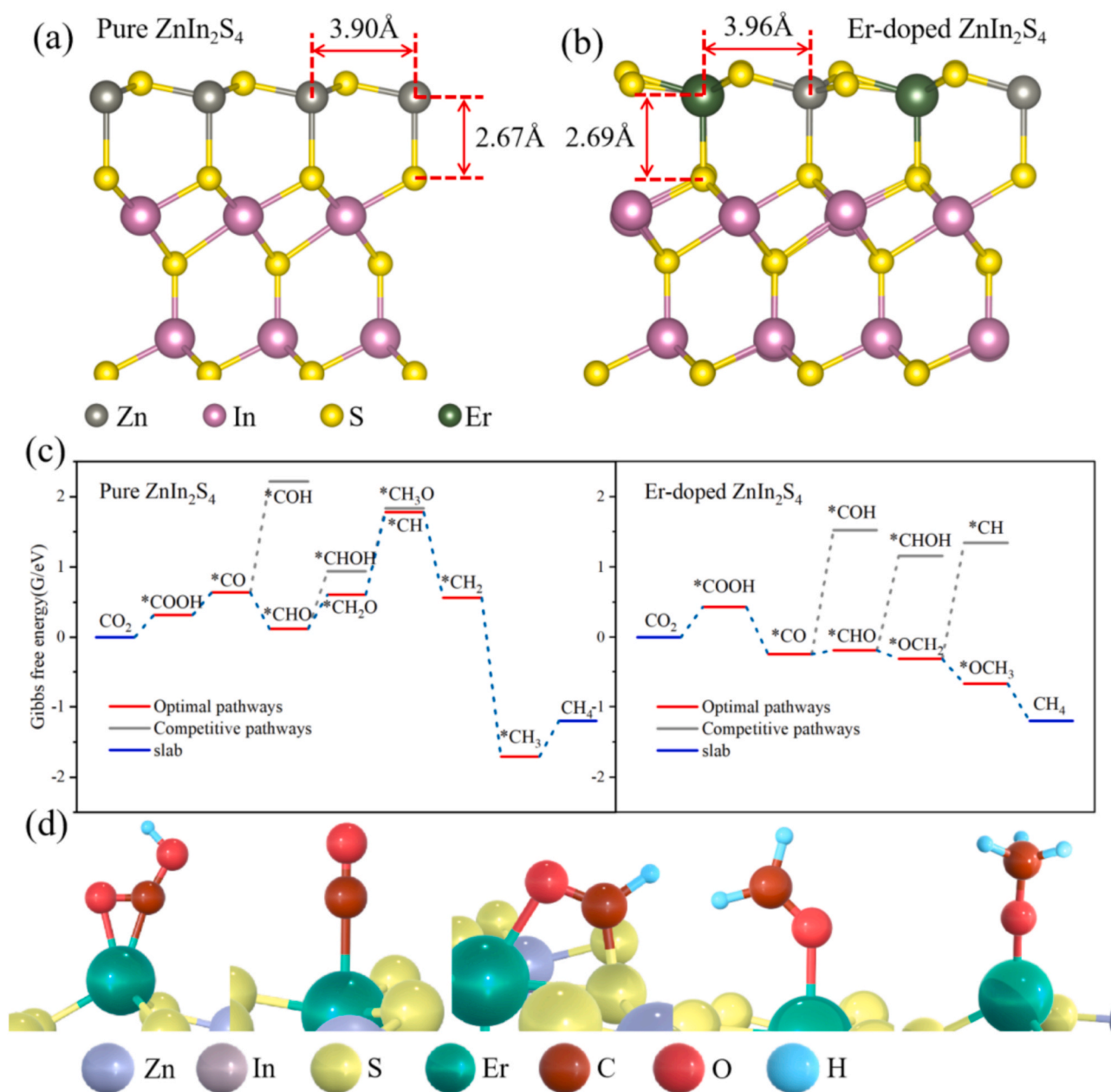


Fig. 8. Adsorbed CO₂ slab model (a, b), free energy diagram for CO₂ reduction (c), and adsorbed intermediate states on the surface of Er-doped ZnIn₂S₄ (d).

structure of the valence band. In the valence band region, the localized 4 f orbitals of Er display notable hybridization with the orbitals of other elements, generating the observed divergence in the band structure [33].

In this study, we utilize the Electron Localization Function (ELF) to shed light on the changes induced by doping Er into the ZnIn₂S₄ system [34]. The ELF acts as a quantitative measure of the probability of locating an electron in the vicinity of another electron with the same spin, thereby allowing us to comprehensively analyze the effects of Er-doping on the electronic structure and bonding configurations in the ZnIn₂S₄ matrix. In the ELF maps, the colors red and blue correspond to the highest (1.0) and lowest (0.0) ELF values respectively, signifying regions of electron accumulation and depletion. It can be seen from Fig. 6e, f that when the central Zn is replaced with Er, the ELF values in the surrounding areas increase to around 0.5. This denotes a significant increase in the electron localization around Er, with the electron distribution becoming more concentrated in this region. This change

highlights an enhanced electron interaction between Er and the surrounding atoms, indicating a potential shift in electronic and optoelectronic properties of the doped system.

3.4. Photocatalytic CO₂ reduction mechanism

In situ Diffuse Reflectance Infrared Fourier Transform Spectroscopy (DRIFTS) was employed to probe the reaction intermediates during the photocatalytic reduction of CO₂ (Fig. 7). After preheating the samples at 80 °C for 4 h, CO₂ adsorption was performed in a dark environment, as represented by the blue series of lines in the figure. Following 30 min of adsorption in dark conditions, distinct absorption peaks corresponding to monodentate carbonate species (m-CO₃) and bidentate carbonate species (b-CO₃) were prominently observed for both pure ZnIn₂S₄ (PZ) and Er-doped ZnIn₂S₄ (3EZ). These peaks signify effective adsorption and activation of CO₂ and H₂O on the surface of the samples [35]. Upon illumination, new absorption peaks emerged while the original

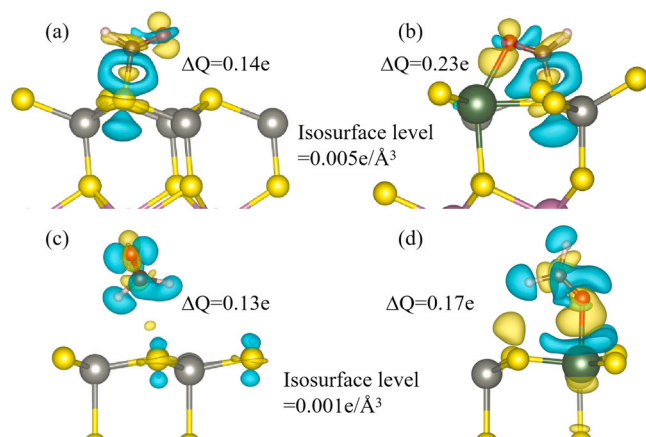


Fig. 9. Differential charge density of $^*\text{CHO}/^*\text{CH}_2\text{O}$ adsorption on (a/c) ZnIn_2S_4 , (b/d) $\text{Er-ZnIn}_2\text{S}_4$.

carbonate species peaks dissipated. In the case of $\text{Er-ZnIn}_2\text{S}_4$, peaks at 962, 1043, and 1530 cm^{-1} could be attributed to $^*\text{CHO}$, $^*\text{OCH}_3$, and $^*\text{COOH}$ species, respectively [36]. These species are generated from CO_2 and $-\text{OH}$ groups and serve as key intermediates for subsequent CH_4 production. Both samples exhibited absorption peaks for $^*\text{CH}_2$ groups at 2856 and 2935 cm^{-1} , suggesting that the reduction products for PZ and 3EZ samples are inclined toward CH_4 [37]. Notably, the 3EZ sample demonstrated significantly stronger dissipation of b-CO_3 compared to PZ, which implies a greater capability of 3EZ for CO_2 reduction and accounts for its higher yield. On the other hand, the spectra for 3EZ showed additional peaks between 1210 and 1240 cm^{-1} , which can be assigned to $^*\text{OCH}_2$ groups, indicating a divergent pathway for CO_2 reduction compared to PZ.

To delve further into the promotional effects of $\text{Er-doped ZnIn}_2\text{S}_4$ on the adsorption and catalysis of CO_2 , we conducted detailed calculations on the adsorption behavior of CO_2 on the catalyst surface and the formation of surface species during the reaction process. Upon close observation of the slab surface before and after Er doping, it can be seen that the large atomic radius of Er leads to an increased inter-atomic distance on the surface (Fig. 8a, b). The expanded surface voids offer more active sites for catalytic reactions, thereby enhancing the catalytic activity. By calculating the adsorption energy of CO_2 on the catalyst surface (Fig. S3), we found that the adsorption energy of CO_2 on the $\text{Er-doped ZnIn}_2\text{S}_4$ was -0.41 eV , compared to -0.24 eV on the pristine ZnIn_2S_4 surface. This indicates that $\text{Er-doped ZnIn}_2\text{S}_4$ exhibits a stronger adsorption capability for CO_2 .

Gibbs free energy calculations of the reaction process enable us to determine the distinct reduction pathways of CO_2 on the catalyst surface (Fig. 8c). On the pristine ZnIn_2S_4 surface, the minimum energy barrier pathway for CO_2 reduction to CH_4 is: $\text{CO}_2 \rightarrow ^*\text{COOH} \rightarrow ^*\text{CO} \rightarrow ^*\text{CHO} \rightarrow ^*\text{CH}_2\text{O} \rightarrow ^*\text{CH} \rightarrow ^*\text{CH}_2 \rightarrow ^*\text{CH}_3 \rightarrow \text{CH}_4$. Conversely, on the Er-doped catalyst surface, the formation of the coordination bond between O and Er has a lower bond energy, facilitating the generation of $^*\text{OCH}_3$ surface species. Its specific reduction pathway is: $\text{CO}_2 \rightarrow ^*\text{COOH} \rightarrow ^*\text{CO} \rightarrow ^*\text{CHO} \rightarrow ^*\text{OCH}_2 \rightarrow ^*\text{OCH}_3 \rightarrow \text{CH}_4$. These two different reaction pathways result in a substantial difference in reaction barriers. The energy barrier for reduction on the pristine ZnIn_2S_4 surface is 1.17 eV , with the rate-determining step being $^*\text{CH}_2\text{O} \rightarrow ^*\text{CH}$. On the $\text{Er-doped ZnIn}_2\text{S}_4$ surface, the energy barrier for reduction is 0.43 eV , with the rate-determining step being $\text{CO}_2 \rightarrow ^*\text{COOH}$. This renders CO_2 reduction on the $\text{Er-doped ZnIn}_2\text{S}_4$ surface more facile, corroborating the superior performance of the doped catalyst for CO_2 reduction observed in our experiments.

Another crucial metric for evaluating the performance of catalysts in CO_2 reduction is their capability to suppress the Hydrogen Evolution Reaction (HER) [38]. Although experimental evidence has confirmed

the inhibitory potential of $\text{Er-doped ZnIn}_2\text{S}_4$ towards HER, we further calculated the Gibbs free energy for HER separately (Fig. S4). The results show that the reaction barriers for HER on the pristine ZnIn_2S_4 and $\text{Er-doped ZnIn}_2\text{S}_4$ surfaces are 0.63 eV and 1.18 eV , respectively. The higher barrier on the $\text{Er-doped ZnIn}_2\text{S}_4$ surface confirms its superior efficacy in suppressing the HER process.

In the CO_2RR to CH_4 , the hydrogenation of $^*\text{CO}$ to $^*\text{CH}_x\text{O}$ is deemed as a crucial step dictating selectivity [39]. By examining the optimal pathways on ZnIn_2S_4 before and after Er doping, it is found that $^*\text{CHO}$ and $^*\text{CH}_2\text{O}$ serve as key intermediates. As a result, to explore the reason why $\text{Er-doped ZnIn}_2\text{S}_4$ demonstrates such high selectivity compared to pure ZnIn_2S_4 in the CO_2 reduction to CH_4 , we performed differential charge density and Bader charge analyses to investigate the charge transfer during the adsorption of $^*\text{CHO}$ and $^*\text{CH}_2\text{O}$ on the surfaces of these two catalysts [40]. We define ΔQ as the sum of the absolute values of Bader charge differences, quantifying the extent of charge transfer. A larger ΔQ implies a higher degree of charge transfer. As illustrated in Fig. 9, the blue regions represent charge depletion, while the yellow areas indicate charge accumulation. Through the charge calculation of $^*\text{CHO}$, it was found that during adsorption on the pure ZnIn_2S_4 surface, although O accumulates some charge, C and H lose charge with a total charge transfer (ΔQ) of $0.14e$. Conversely, on the $\text{Er-doped ZnIn}_2\text{S}_4$ surface, the introduction of Er enhances the catalyst's ability to transfer charge to oxygen, elevating ΔQ to $0.23e$, thereby achieving stable adsorption of the key intermediate. For $^*\text{CH}_2\text{O}$, due to the strong bonding interaction between O and Er, ΔQ on the surface of $\text{Er-doped ZnIn}_2\text{S}_4$ is also higher than that on pure ZnIn_2S_4 , exhibiting a stronger adsorption effect.

4. Conclusion

In summary, we successfully synthesized $\text{Er-doped ZnIn}_2\text{S}_4$ using a hydrothermal method. Despite its similar morphology to that of pure ZnIn_2S_4 , XRD and XPS characterization results demonstrated that erbium doping did not adversely affect the original structure of ZnIn_2S_4 . Through DFT calculations, we confirmed that the incorporation of erbium introduced new energy levels, effectively narrowing the band gap. These changes played a decisive role in enhancing the efficiency and selectivity of its photocatalytic CO_2 reduction. We found that, similar to most materials, pure ZnIn_2S_4 tends to form coordinate bonds with C during the CO_2 adsorption reduction process, whereas erbium-doped ZnIn_2S_4 prefers to form coordinate bonds with O. This discovery reveals that erbium-doped ZnIn_2S_4 provides a completely new, lower-barrier reduction pathway for CO_2 , which well explains why erbium-doped ZnIn_2S_4 has a higher reduction efficiency. We have discovered that $\text{Er-ZnIn}_2\text{S}_4$ provides a more stable adsorption platform for the key intermediate, $^*\text{CHO}$ and $^*\text{CH}_2\text{O}$, in the reduction of CO_2 to CH_4 . This lends theoretical support for achieving high selectivity. These results provide valuable theoretical and practical basis for the design and development of efficient and selective photocatalysts.

CRedit authorship contribution statement

Fanghe Zhou: First Author, responsible for Investigation, Methodology, establishment of DFT models, and manuscript Writing – original draft. **Yongling Zhang:** First Author, responsible for Sample Preparation, Experimental Characterization, Formal analysis, and manuscript revisions (original draft). **Jiang Wu*:** Corresponding Author, responsible for Supervision, Project administration, Funding acquisition, and manuscript revisions. **Wu Yang:** Experimental Characterization. **Xu Fang:** Software. **Tao Jia:** Formal analysis, Validation, and manuscript revisions. **Yang Ling:** Formal analysis, Validation, and manuscript revisions. **Ping He:** Formal analysis, Validation. **Qizhen Liu*:** Corresponding Author, Supervision. **Jia lin*:** Corresponding Author, Supervision.

Declaration of Competing Interest

This manuscript is original. All authors have approved the submission of the manuscript. This article has not been published and is not being considered for publication elsewhere.

Data availability

Data will be made available on request.

Acknowledgement

This work was partially sponsored by National Natural Science Foundation of China (52076126), Science and Technology Committee of Shanghai Municipality (22dz1208800), and Shanghai Science and Technology Committee (22010501500), Key Laboratory of Clean Power Generation and Environmental Protection Technology in Mechanical Industry.

Appendix A. Supporting information

Supplementary data associated with this article can be found in the online version at [doi:10.1016/j.apcatb.2023.123347](https://doi.org/10.1016/j.apcatb.2023.123347).

References

- [1] Z. Zhang, S.Y. Pan, H. Li, et al., Recent advances in carbon dioxide utilization, *Renew. Sustain. Energy Rev.* 125 (2020), 109799.
- [2] W. Tu, Y. Zhou, Z. Zou, Photocatalytic conversion of CO₂ into renewable hydrocarbon fuels: state-of-the-art accomplishment, challenges, and prospects, *Adv. Mater.* 26 (27) (2014) 4607–4626.
- [3] O.K. Varghese, M. Paulose, T.J. LaTempa, et al., High-rate solar photocatalytic conversion of CO₂ and water vapor to hydrocarbon fuels, *Nano Lett.* 9 (2) (2009) 731–737.
- [4] S. Wang, L. Yi, J.E. Halpert, et al., A novel and highly efficient photocatalyst based on P25-graphdiyne nanocomposite, *Small* 8 (2) (2012) 265–271.
- [5] L. Wang, B. Cheng, L. Zhang, et al., In situ irradiated XPS investigation on S-scheme TiO₂@ ZnIn₂S₄ photocatalyst for efficient photocatalytic CO₂ reduction, *Small* 17 (41) (2021), 2103447.
- [6] J. Wang, S. Sun, R. Zhou, et al., A review: synthesis, modification and photocatalytic applications of ZnIn₂S₄, *J. Mater. Sci. Technol.* 78 (2021) 1–19.
- [7] T. Jia, Z. Ji, J. Wu, et al., Nanosized ZnIn₂S₄ supported on facet-engineered CeO₂ nanorods for efficient gaseous elemental mercury immobilization, *J. Hazard. Mater.* 419 (2021), 126436.
- [8] C. Li, H. Che, Y. Yan, et al., Z-scheme AgVO₃/ZnIn₂S₄ photocatalysts: “One Stone and Two Birds” strategy to solve photocorrosion and improve the photocatalytic activity and stability, *Chem. Eng. J.* 398 (2020), 125523.
- [9] M.S. Hassan, T. Amna, O.B. Yang, et al., TiO₂ nanofibers doped with rare earth elements and their photocatalytic activity, *Ceram. Int.* 38 (7) (2012) 5925–5930.
- [10] *The Rare Earth Elements: Fundamentals and Applications*, John Wiley & Sons, 2013.
- [11] Z.S. Liu, Z.L. Liu, J.L. Liu, et al., Enhanced photocatalytic performance of Er-doped Bi₂WO₆/Bi₂VO₆: facile synthesis and photocatalytic mechanism, *Mater. Res. Bull.* 76 (2016) 256–263.
- [12] R.G. Wilson, R.N. Schwartz, C.R. Abernathy, et al., 1.54-μm photoluminescence from Er-implanted GaN and AlN, *Appl. Phys. Lett.* 65 (8) (1994) 992–994.
- [13] M. Achehboune, M. Khenfouch, I. Boukhoubza, et al., A DFT study on the electronic structure, magnetic and optical properties of Er doped ZnO: effect of Er concentration and native defects, *Comput. Condens. Matter* 31 (2022), e00627.
- [14] J. Wang, D. Wang, X. Zhang, et al., An anti-symmetric dual (ASD) Z-scheme photocatalytic system: (ZnIn₂S₄/Er³⁺: Y₃Al₅O₁₂@ ZnTiO₃/CaIn₂S₄) for organic pollutants degradation with simultaneous hydrogen evolution, *Int. J. Hydrog. Energy* 44 (13) (2019) 6592–6607.
- [15] W. Wang, R. Dai, L. Zhang, et al., Experimental and DFT investigation on the different effects of Er³⁺- and Ag⁺-doped BiOBr microspheres in enhancing photocatalytic activity under visible light irradiation, *J. Mater. Sci.* 55 (2020) 11226–11240.
- [16] M. Achehboune, M. Khenfouch, I. Boukhoubza, et al., A DFT study on the electronic structure, magnetic and optical properties of Er doped ZnO: effect of Er concentration and native defects, *Comput. Condens. Matter* 31 (2022), e00627.
- [17] C. Kim, F. Dionigi, V. Beermann, et al., Alloy nanocatalysts for the electrochemical oxygen reduction (ORR) and the direct electrochemical carbon dioxide reduction reaction (CO₂RR), *Adv. Mater.* 31 (31) (2019), 1805617.
- [18] Y. Ling, J. Li, C. Zou, et al., Interaction mechanism between gaseous arsenic and the unburned carbon in coal-fired fly ash: a DFT combined thermodynamics study, *Chem. Eng. J.* 425 (2021), 130714.
- [19] V. Wang, N. Xu, J.C. Liu, et al., VASPKIT: a user-friendly interface facilitating high-throughput computing and analysis using VASP code, *Comput. Phys. Commun.* 267 (2021), 108033.
- [20] U. Holzwarth, N. Gibson, The Scherrer equation versus the ‘Debye-Scherrer equation’, *Nat. Nanotechnol.* 6 (9) (2011), 534–534.
- [21] G. Wang, Z. Luo, Q. Wei, et al., Dual-metal sites CuInS₂/g-C₃N₄ Z-scheme heterojunction with efficient photocatalytic CO₂ reduction selectivity, *Fuel Process. Technol.* 238 (2022), 107530.
- [22] S.A. Speakman, Estimating crystallite size using XRD, *MIT Cent. Mater. Sci. Eng.* 2 (2014) 14.
- [23] G. Yang, D. Chen, H. Ding, et al., Well-designed 3D ZnIn₂S₄ nanosheets/TiO₂ nanobelts as direct Z-scheme photocatalysts for CO₂ photoreduction into renewable hydrocarbon fuel with high efficiency, *Appl. Catal. B Environ.* 219 (2017) 611–618.
- [24] S. Jeon, P.V. Braun, Hydrothermal synthesis of Er-doped luminescent TiO₂ nanoparticles, *Chem. Mater.* 15 (6) (2003) 1256–1263.
- [25] L. Liang, X. Li, J. Zhang, et al., Efficient infrared light induced CO₂ reduction with nearly 100% CO selectivity enabled by metallic CoN porous atomic layers, *Nano Energy* 69 (2020), 104421.
- [26] A.Y. Lee, A.S. Myerson, Particle engineering: fundamentals of particle formation and crystal growth, *MRS Bull.* 31 (11) (2006) 881–886.
- [27] S. Wang, B.Y. Guan, X.W.D. Lou, Construction of ZnIn₂S₄-In₂O₃ hierarchical tubular heterostructures for efficient CO₂ photoreduction, *J. Am. Chem. Soc.* 140 (15) (2018) 5037–5040.
- [28] S. Si, H. Shou, Y. Mao, et al., Low-coordination single Au atoms on ultrathin ZnIn₂S₄ nanosheets for selective photocatalytic CO₂ reduction towards CH₄, *Angew. Chem.* 134 (41) (2022), e202209446.
- [29] Z. Lian, F. Wu, J. Zi, et al., Infrared light-induced anomalous defect-mediated plasmonic hot electron transfer for enhanced photocatalytic hydrogen evolution, *J. Am. Chem. Soc.* (2023).
- [30] J. Hafner, Ab-initio simulations of materials using VASP: density-functional theory and beyond, *J. Comput. Chem.* 29 (13) (2008) 2044–2078.
- [31] A. Khataee, S. Arefi-Oskoui, M. Fathinia, et al., Synthesis, characterization and photocatalytic properties of Er-doped PbSe nanoparticles as a visible light-activated photocatalyst, *J. Mol. Catal. A Chem.* 398 (2015) 255–267.
- [32] E. Cerrato, E. Gaggero, P. Calza, et al., The role of cerium, europium and erbium doped TiO₂ photocatalysts in water treatment: a mini-review, *Chem. Eng. J. Adv.* 10 (2022), 100268.
- [33] S. Vijay, W. Ju, S. Brückner, et al., Unified mechanistic understanding of CO₂ reduction to CO on transition metal and single atom catalysts, *Nat. Catal.* 4 (12) (2021) 1024–1031.
- [34] H. Zhang, Y. Li, J. Hou, et al., FeB₆ monolayers: the graphene-like material with hypercoordinate transition metal, *J. Am. Chem. Soc.* 138 (17) (2016) 5644–5651.
- [35] L. Wang, B. Cheng, L. Zhang, et al., In situ irradiated XPS investigation on S-scheme TiO₂@ ZnIn₂S₄ photocatalyst for efficient photocatalytic CO₂ reduction, *Small* 17 (41) (2021), 2103447.
- [36] J. Li, H. Huang, W. Xue, et al., Self-adaptive dual-metal-site pairs in metal-organic frameworks for selective CO₂ photoreduction to CH₄, *Nat. Catal.* 4 (8) (2021) 719–729.
- [37] S. Bai, W. Jing, G. He, et al., Near-infrared-responsive photocatalytic CO₂ conversion via in situ generated Co₃O₄/Cu₂O, *ACS Nano* (2023).
- [38] A. Goyal, G. Marcandalli, V.A. Mints, et al., Competition between CO₂ reduction and hydrogen evolution on a gold electrode under well-defined mass transport conditions, *J. Am. Chem. Soc.* 142 (9) (2020) 4154–4161.
- [39] J. Zhao, P. Zhang, T. Yuan, et al., Modulation of *CH₃O adsorption to facilitate electrocatalytic reduction of CO₂ to CH₄ over Cu-based catalysts, *J. Am. Chem. Soc.* 145 (12) (2023) 6622–6627.
- [40] M. Yu, D.R. Trinkle, Accurate and efficient algorithm for Bader charge integration, *J. Chem. Phys.* 134 (6) (2011).